analytical chemistry

pubs.acs.org/ac Article

Flexible Drift Tube for High Resolution Ion Mobility Spectrometry (Flex-DT-IMS)

Barry L. Smith, Cedric Boisdon, Iain S. Young, Thanit Praneenararat, Tirayut Vilaivan, and Simon Maher*

Cite This: *Anal. Chem.* 2020, 92, 9104–9112

Read Online

ACCESS | Metrics & More | Article Recommendations | Supporting Information

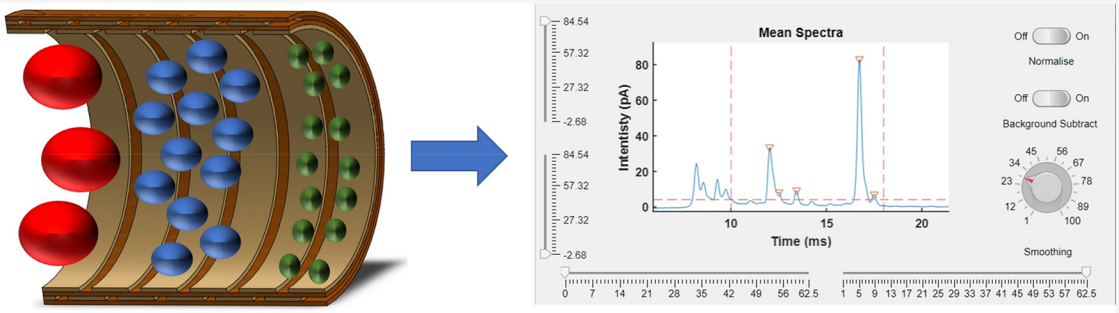

ABSTRACT: This paper describes, in detail, the development of a novel, low-cost, and flexible drift tube (DT) along with an associated ion mobility spectrometer system. The DT is constructed from a flexible printed circuit board (PCB), with a bespoke "dog-leg" track design, that can be rolled up for ease of assembly. This approach incorporates a shielding layer, as part of the flexible PCB design, and represents the minimum dimensional footprint conceivable for a DT. The low thermal mass of the polyimide substrate and overlapping electrodes, as afforded by the dog-leg design, allow for efficient heat management and high field linearity within the tube—achieved from a single PCB. This is further enhanced by a novel double-glazing configuration which provides a simple and effective means for gas management, minimizing thermal variation within the assembly. Herein, we provide a full experimental characterization of the flexible DT ion mobility spectrometer (Flex-DT-IMS) with corresponding electrodynamic (Simion 8.1) and fluid dynamic (SolidWorks) simulations. The Flex-DT-IMS is shown to have a resolution >80 and a detection limit of low nanograms for the analysis of common explosives (RDX, PETN, HMX, and TNT).

Atmospheric pressure drift tube ion mobility spectrometry (DT-IMS) is a well-established and powerful analytical technique that is fast (~micro to milliseconds) and sensitive (typically < ~low ppb) for the detection of gas phase analyte ions of interest. Measuring time-of-flight (ToF) and hence the velocity of ion packets, drifting in a homogeneous electric field of known length, enables acquisition of spectra relating to the individual analyte ion mobilities (eq 1),

$$K = \frac{v_d}{E} \tag{1}$$

where v_d is the drift velocity (cm/s), E is the electric field strength (V/cm) and K is the ion mobility ($cm^2/(V\ s)$). To allow direct comparison between different instruments and operating parameters, reduced ion mobility (K_0) is often reported which takes into account normalized temperature and pressure of the drift region (eq 2),

$$K_0 = K\left(\frac{T_0}{T}\right)\left(\frac{P}{P_0}\right) \tag{2}$$

where T_0 is standard temperature (273.15 K), T is drift gas temperature (K), P is operating pressure (Torr) and P_0 is standard pressure (760 Torr). Comparisons can be drawn between DT-IMS and ToF-mass spectrometry (MS), however, unlike MS, DT-IMS measurements are made at atmospheric pressure thus vastly reducing the requirement for auxiliary equipment, in particular vacuum pumps.[1] This advantage (with subsequent implications for robustness and portability) is a key reason why IMS instruments have proven the most effective and widely used technology for trace detection of explosives,[2−5] narcotics[6,7] and chemical warfare agents[8] in field-deployable scenarios such as battlefields and/or border security installations. For instance, swabs taken from clothing, luggage, and/or passengers at an airport facility are typically analyzed

Received: March 28, 2020
Accepted: June 1, 2020
Published: June 1, 2020

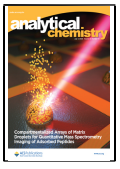

via thermal desorption with the resultant neutral vapors acquiring charge via ionizing radiation prior to analysis by a DT-IMS instrument. More recently DT-IMS has enjoyed the attention of structural biologists interested in native analysis of lipids[9] and proteins.[10,11]

The major limitation of IMS is its typically low resolving power. For IMS, the resolution or resolving power, R_P, can be defined as the drift time, t_d, divided by the peak width at half-maximum, $w_{0.5}$, and can be broadly thought of as the ability of the instrument to separate chemical species of similar mobilities (eq 3),

$$R_P = \frac{t_d}{w_{0.5}} \tag{3}$$

More detailed equations for IMS resolution have been derived previously.[12] One such expression for estimating resolving power, R_P, is given in eq 4, which places two fundamental limitations on the resolving power of an IMS instrument as described by Kirk et al.,[13]

$$R_P = \sqrt{\frac{1}{\left(\frac{w_{min} K U_D}{L^2}\right)^2 + \frac{16 k_B T \ln(2)}{z e U_D}}} \tag{4}$$

where w_{min}, is the minimum injection width of the ion packet into the drift tube; K, is the mobility of the ion under investigation; U_D, is the drift tube voltage; L, is the drift tube length; T, is the drift tube temperature, and, k_B, z, and e are constants: Boltzmann, ion charge state (typically +1) and electron charge. The left-hand denominator in eq 4 is the contribution from the "minimum-width-limit" and the right-hand denominator relates to "diffusion-limited" resolving power.

A great deal of research effort has focused on developing high resolution (R_P > 80)[14−16] and ultrahigh resolution ion mobility instruments (R_P > 200).[17,18] Recent advancements have largely been achieved by increasing the drift voltage applied across longer drift tubes,[19] along with improvements in ion shutter technology[20−22] that allow ions to be pulsed into the drift region with smaller packet widths. Further increases in resolving power have been achieved by advanced signal processing algorithms[23] allowing resolving powers in excess of 400 to be achieved. Commercially available instruments, such as those typically used at border control installations, generally have resolving powers of ∼50 which is sufficient for resolving most explosive compounds with satisfactory certainty.[18]

The key component of a DT IMS instrument is, of course, the drift tube. The primary objective of the DT design is the establishment of an idealized homogeneous electric field. Additionally, ease of assembly, maintenance and interfacing to other IMS subsystems such as the detector, heater and ion gate influence the design and construction methods. Early DTs had metallic conductors held together under spring tension with sapphire balls providing insulation between the conductive electrodes.[24] These were later replaced by Macor insulating rings to prevent any molecules from residing in the drift tube enclosure which could escape from the gaps between the conductive electrodes and then re-enter the drift region creating issues such as chemical noise and peak broadening.

Soppart and Baumbach[25] established two important criteria for forming high quality fields inside DTs: (i) the ratio of electrode thickness to DT inner diameter should be minimized, ideally below 1:10, and, (ii) the distance between rings should also be minimized to effectively decouple the internal field from any grounded enclosure surrounding the DT. Liu et al.[26] found that discontinuities in the field shape, caused by orthogonal fields introduced from the gate and detector at the extremes of the DT, could be eliminated by optimizing the electrode thickness and spacing of each electrode along the DT. Hauck et al.[27] recently developed a hermetically sealed DT with outstanding K_0 accuracy which consisted of insulators and metallic electrodes that were well matched in terms of thermal expansion coefficients (<0.1 ppm/°C). Nevertheless, the basic design of DTs in use in the scientific literature and within commercially available IMS systems has largely remained unchanged.

The most widely reported exception to this trend is a resistive glass DT patented by Laparde[28] and implemented and evaluated by Kwasnick et al.,[29,30] whereby a linear field gradient is established by applying a high voltage across a resistive glass tube with resistance similar to typical, conventional DT design (∼0.4 GΩ). This monolithic design was reported to enable simpler construction and enhance uniformity of the field. Hollerbach et al. cleverly devised an extruded 3-D printed DT containing multiwalled carbon nanotubes to enable electrical conduction in an otherwise insulating polymer.[31] Other notable attempts have also been reported that deviate from the standard design as described in various patents but to our knowledge have not been evaluated in the scientific literature. Drumheller patented[32] a resistive film that could be coated on the interior of a tube in a helical pattern to generate a field gradient with all the associated benefits of a monolithic design. More recently, a self-shielding printed circuit board (PCB) DT design was developed[33] by bonding multiple layers of electrodes on a polyimide substrate material with an adhesive, which can then be rolled up and further bonded to form a fixed DT IMS. This design virtually eliminates any influence from nearby grounded enclosures, which is known to have a significant influence on field quality as previously reported by Soppart and Baumbach.[25]

Utilization of PCB fabrication technology in construction of ion guidance and ion detection systems is becoming increasing widespread.[34−38] Improvements in process control, manufacturing tolerances, and economies of batch processing make it an attractive alternative to more conventional machining for the construction of ion guidance electrodes. Typically, conductive electrodes are machined from pieces of stainless steel or other metals. Voltages applied to the machined electrodes create an electric field that affects the motion of charged particles. Providing the outer surface of an electrode is fully conductive, an internal substructure can be insulating and achieve the same field quality as conventional electrodes. For instance, Reinecke & Clowers[4] implemented a classic stacked ring DT-IMS system entirely constructed from PCBs which, while conceptually simple, requires a substantial amount of postproduction assembly to construct the DT from the individual circuit boards. Additionally, Tridas et al. introduced a novel flex-PCB based RF ion funnel that could be rolled from a flat sheet into a funnel shape with consecutively narrowing electrode diameters.[39]

Herein we report, for the first time, the novel design and construction of a DT IMS constructed from a flexible PCB, with a bespoke "dog-leg" track design, that can be rolled up for ease of assembly. Full experimental characterization of the key features and supporting electrodynamic and fluid dynamic

https://dx.doi.org/10.1021/acs.analchem.0c01357
Anal. Chem. 2020, 92, 9104−9112

simulations are given. Following the evaluation of the Flex-DT-IMS we demonstrate applicability for the analysis of some common explosive compounds (TNT, RDX, HMX, and PETN) with two ion sources: electrospray ionization (ESI) and desorption atmospheric pressure chemical ionization (DAPCI).

EXPERIMENTAL SECTION

Flex-DT-IMS with "Dog-Leg" Shielding Electrodes. In our design we use Kapton as a flexible substrate material for the PCB instead of rigid FR4 substrate (a glass-reinforced epoxy laminate material). A 150 μm single layer of copper (which will form the electrodes) is deposited onto a 300 μm layer of Kapton. The DT is constructed from a single flexible PCB without any requirement for bonding any additional layers. This provides several key advantages for the DT design: (1) All electrodes are deposited on the same piece of substrate (in addition to pick and place of any desired electronic components); that is to say, the DT arrives as a single piece with minimal assembly requirements. (2) The width of the electrodes can be varied continuously as opposed to using FR4 base which typically has discrete thicknesses ranging from 0.2 mm to 3.2 mm. (3) The track width and gap spacings can be very tightly controlled, tolerances as low as $\pm$1 μm are common, enabling creation of highly linear drift fields. (4) Kapton itself has properties that make it an ideal dielectric for IMS applications. It is highly chemically resistant, has a large operating temperature range (−200 to 300 °C) and has thermal expansion properties in accordance with copper, limiting internal stresses when operating at elevated temperatures.

A flexible PCB is designed on a single sheet of Kapton and patterned with a gold-plated copper track layout. A "dog-leg" arrangement allows the flexible substrate to be coiled up without any external reference point other than itself. The kink of the "dog-leg" ensures that when the flexible PCB is rolled up more than once, the overlapping electrodes are situated such that their geometric center is aligned with the center of the dielectric gap separating two adjacent electrodes in the previous layer. Figure 1 shows the phases of construction of the Flex-DT. In practice, the custom flexible PCB design can be ordered from any suitable PCB manufacturer and will arrive as a flat sheet of Kapton with the gold-plated copper electrodes deposited onto the surface as specified (Figure 1(a)). Each track is "dog-legged" at the midpoint such that, when coiled into a tube, the outer electrodes improve the field homogeneity by providing a layer of shielding for the drift electrodes from the influence of any external stray fields in the vicinity (Figure 1(a), insert). By coiling the PCB around a suitably sized tubular object, a symmetrical DT design can be readily achieved within minutes (Figure 1(b)). A cut away view of the final electrode arrangement can be observed in Figure 1(c) with the overlap magnified in Figure 1(d).

The final construction, effectively, consists of four layers: two layers of gold-plated copper electrodes sandwiched between two layers of insulating Kapton substrate. A small amount of nonpermanent adhesive or a mechanical fixing can be used to set the coiled tube in place and, once set, the design is mechanically rigid but can also be readily released for cleaning/maintenance purposes. Both the desolvation and drift region are constructed from the same, single flexible PCB, enabling the manufacture of the whole DT region to be completed within minutes. Omitted from Figure 1 are resistors

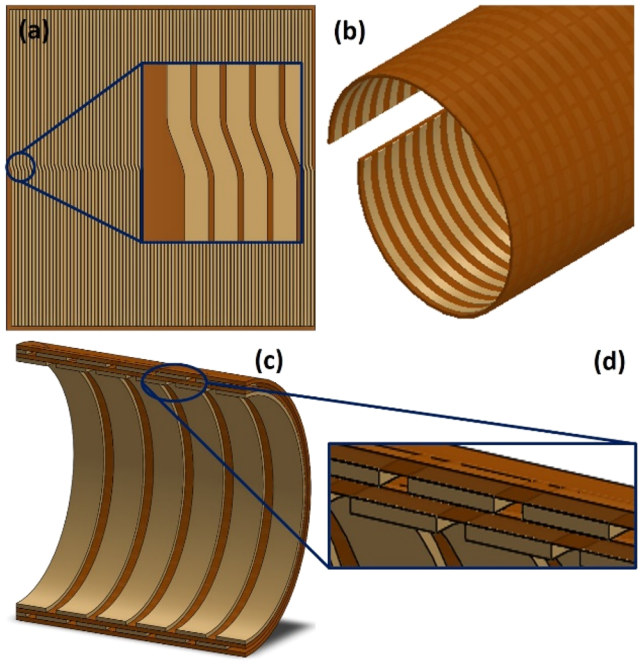

Figure 1. (a) CAD illustration of the flexible drift tube prior to rolling; the inset magnifies the "dog-leg" arrangement. (b) Coiling process. (c) Section view of the finished drift tube showing the drift and shielding electrode arrangement. (d) Magnified view of the overlapping arrangement.

presoldered onto pads at the end of the electrodes at a suitable fabrication facility, using a highly precise, automated pick and place process (which is very common for PCB manufacture), further speeding up assembly time. An additional benefit when using an increased number of thin electrodes is that it allows the use of a large number of lower value resistors (e.g., 100 kΩ vs typical ∼1 MΩ) with improved tolerance (e.g., 0.01% vs typical 0.1%), without power supply loading.

DT and Ion Source HV Power Supplies. Power for the Flex-DT is provided by a variable high voltage power supply (HV-PSU) (Leybold). The sample inlet region is held at ground potential while the Faraday detector plate and associated electronics are connected to the high voltage output of the HV-PSU. Ionization potential (0−6 kV) is provided by a HV module (XPEMCO, XP Power) and user controllable through a potentiometer mounted in the IMS enclosure.

Bradbury−Nielsen (B−N) Gate and Aperture Grids. A custom manufactured B−N gate was constructed for the purpose of gating ions into the DT. 60 μm gold plated molybdenum wire was laid across pretensioned FR4 plates. Each plate had slots cut-in to set the wire spacing at exactly 1.6 mm apart with one plate having slots offset by 0.8 mm. The inner diameter of the FR4 plate was 22 mm giving a total optical transparency of 90%. An electronic switching circuit brings both wires to the same potential to maintain a linear drift gradient during the gate opening time and applies an orthogonal field ($\pm$ 100 V) to inhibit ion passage during closed gate periods. The same method was used to construct an aperture grid placed in front of the Faraday detector.

Temperature and Gas Flow Control. Independent control of desolvation and DT temperatures was achieved using two on−off electronic thermostats (RS, UK). Polyimide-insulated flexible heat pads were used to provide a temperature range from ambient to 110 °C. The desolvation tube heater

https://dx.doi.org/10.1021/acs.analchem.0c01357
Anal. Chem. 2020, 92, 9104−9112

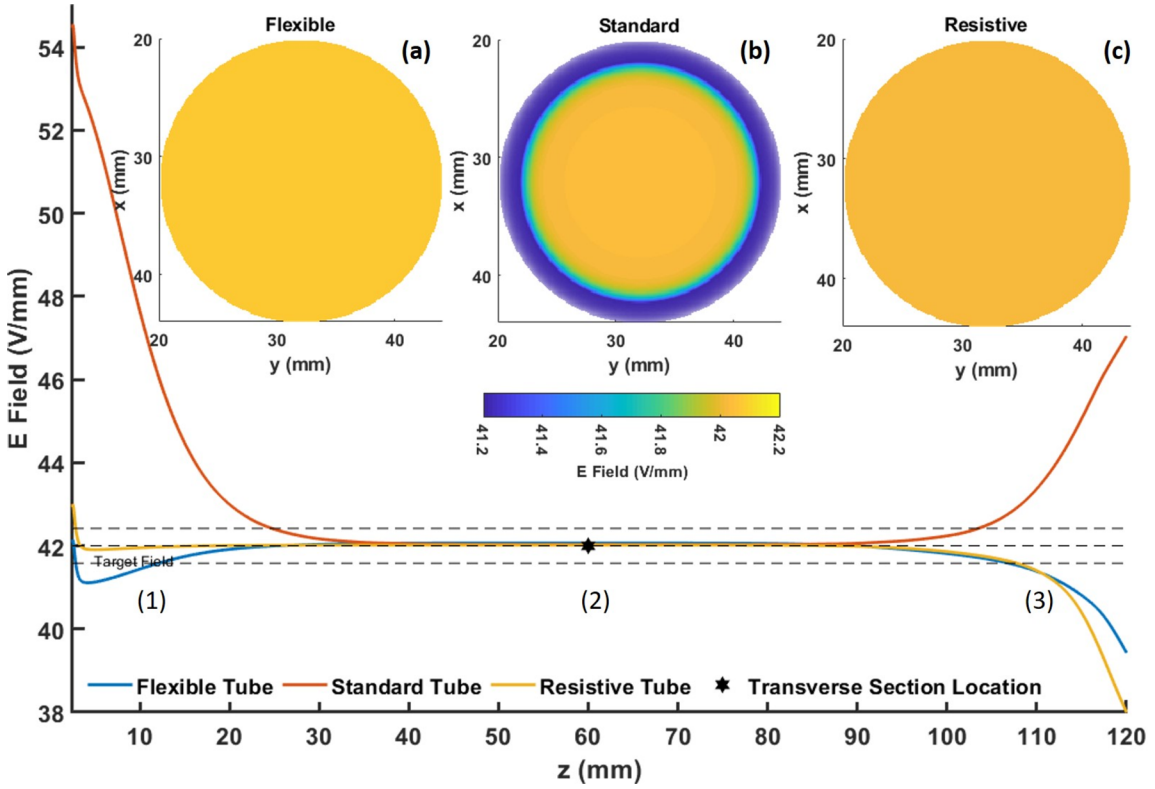

Figure 2. Longitudinal Electric Field plot in V/mm along the drift region. Inserts are transverse electric field plots in V/mm at the center point of the drift region (z = 60 mm) with diameter of 22 mm. The star indicates the center point of the drift region (z = 600 mm), where the cross-sectional (i.e., transverse) distribution of the electric field was taken (as shown in the inset): (a) Flex-DT design, (b) standard stacked ring DT design, (c) monolithic, resistive glass DT design.

was in direct contact with the desolvation tube. Temperature measurement was achieved via a 100 Ω varistor located at its midpoint. The heating element was located on the outside of the inner glass tube surrounding the DT. The varistor was again placed in direct contact with the DT at its midpoint. N_2 gas entry flow was controlled via a 0−1 L/min variable area flow meter (Brookes Instruments).

Transimpedance Amplifier and Analog-Digital Conversion. A high precision electrometer operational amplifier (ADA4530) provides the main transimpedance gain stage and is directly connected to the Faraday plate. Analog to digital conversion (ADC) is performed after a buffering stage following the transimpedance stage. Bipolar (± 10 V) inputs, 16-bit ADC (LTC2327) performs the conversion with a sampling rate of 500 kS/s. Digitized data is transferred via a fiber optic link to the host MCU which relays the raw spectral data to the PC software.

Data Acquisition and Analysis. All spectra were collected using an in-house developed IMS instrument. A custom MATLAB (MathWorks) GUI handles communications between the PC and the IMS instrument through a USB interface. Real time software signal processing functions enable low pass filtering, averaging and smoothing to the incoming data stream. Automated postprocessing scripts, also written in Matlab, make use of the findpeaks function to detect, characterize and report drift time (ms), peak width (ms), peak height (pA), peak resolution (FWHM) and K_0 (cm^2/(V s)). The Flex-DT-IMS configuration and operating parameters are summarized in the Supporting Information (Table S1).

Simion Simulation Settings. Simion 8.1 was used to generate electric field maps. Briefly, a geometry file (.GEM) was created with adjustable parameters to define the important geometric features for each DT design. Since DT designs are symmetrical around the central axis, a highly resolved 2-D mesh was used to construct the geometry with resolution of 0.1 mm/grid unit (gu). A user program adjusted the potential on each electrode to provide a linear gradient and exported a text file with the (x, y, z) coordinate geometry and associated electric field and potential gradients for postprocessing and visualization in Matlab. No attempt was made to optimize the geometry in relation to the grounded shield, however the distance to it from the DT was constant in each case.

Solidworks Flow Simulator Settings. Hydrodynamic 3D flow vectors are generated using SOLIDWORKS (Solidworks Corp.) flow simulator. The software solves the Navier−Stokes equations for conservation of continuity, momentum and energy within the simulation domain. To elicit the highest possible accuracy, exact dimensions and material properties were assigned to the relevant geometric structures in the simulation model to match the real instrument. The continuity between mechanical design and simulation is enhanced in Solidworks flow simulator as it is embedded within the mechanical design environment, therefore the geometric dimensions are inherently the same. The simulation domain was 15 cm × 5 cm and with planar symmetry employed in the x and y direction. The total cell counts were 4 514 322 individual fluid cells and 4 662 813 solid feature cells and 1 017 480 partial cells. A Cartesian mesh was created with sufficient granularity to ensure a minimum of 5 simulation cells were present across any small channels or features within the model.

https://dx.doi.org/10.1021/acs.analchem.0c01357
Anal. Chem. 2020, 92, 9104−9112

An external simulation was performed with an internal fluid region consisting of an inlet flow boundary of 1000, 800, 600, 400, and 200 mL/min of N_2 gas and static pressure of 760 Torr and an ambient temperature of 25 °C at the external simulation domain boundary. Heat conduction in solids option was enabled to model the heat transfer through the solid material. Two thermostats were defined as the volume of the heating elements and the residual effect of the nonheated material and subsequent effect on the gas flow and temperature profile.

Chemicals and Reagents. All chemicals and reagents used in this study were procured from Sigma-Aldrich (Dorset, UK). 1000 μg/mL analytical chemical standards of RDX, TNT, HMX, and PETN were purchased. Serial dilution was performed to generate a sample set of 1000 ng/mL, 500 ng/mL, 100 ng/mL, 50 ng/mL, and 10 ng/mL for determining a calibration curve. Stock solutions for each explosive solution were made using HPLC grade solvents (ACN for TNT, RDX, and HMX and methanol for PETN). Solid iodine beads were also purchased from Sigma-Aldrich (Dorset, UK).

Experimental Settings. *ESI Settings.* A home-built ESI source was constructed from a syringe pump and pulled glass capillary tip. The inner diameter (ID) of the capillary and the outer diameter (OD) of the needle were matched to enable a good seal when the capillary was slid over the syringe needle. A section of needle was left exposed to connect to the HV supply of the IMS system. An extra step was taken to provide dielectric insulation between syringe pump driver and the syringe under high voltage. For ESI analysis of all explosives, a flow rate of 5 μL/min and spray voltage of −4 kV were applied to the needle tip with the earthed IMS enclosure acting as the ground reference. The tip of the pulled capillary was placed concentrically with, and at a distance of 10 mm from, the IMS inlet. The ESI source was operated within an ambient environment without any nebulizer gas.

DAPCI Settings. DAPCI is an ambient ionization technique that was developed by Cooks group at the same time as the more famous DESI source for direct analysis of solid phase material, typically for applications suited to mass spectrometry.[40] It has formerly been employed for direct analysis of explosives,[41,42] crude oil,[43] and biomedical applications.[44,45] In this article we use a DAPCI source similar to the one described here.[46] Ten μL of 500 ng/mL of RDX, TNT, HMX, and PETN were each pipetted onto separate 2 cm × 5 cm Whatman grade 1 filter paper strips. The sample coverage at the end of the paper strip was approximately 1 cm^2. After allowing to dry, each paper strip was placed on the sampling stage at the IMS inlet for analysis with the DAPCI probe. A schematic for the DAPCI experiment, and further details can be found in Supporting Information Figure S1.

RESULTS AND DISCUSSION

Electric Field Homogeneity. Electric field homogeneity is a fundamental requirement for DT-IMS instruments, as it is the major force governing the motion of ions.[25] It is therefore critical to assess the performance of the Flex-DT in terms of field homogeneity. To evaluate our design, we compare it against the "best-in-class" in terms of field homogeneity, a commercial resistive glass DT design (Photonis, France), as well as a more conventional stacked ring DT using Simion 8.1. Raw equipotential field lines, exported from Simion, are overlaid on a CAD model of the drift tube, as seen in Supporting Information Figure S2 for each case.

Figure 2 shows the electric field strength along the longitudinal z axis. To interpret the graph, we split the axis into three regions: entrance (1), middle (2), and exit (3). In region 1, the resistive glass DT achieves the target field at a distance of 1 mm inside the DT and deviates by less than 0.8 V/mm. Deviation occurs due to the entrance aperture grid modeled as a real electrode with finite thickness (0.8 mm) and wire diameter (0.06 mm), which creates a component of the field orthogonal to the z direction. The gap between the entrance aperture and resistive electrode is small (0.2 mm), therefore convergence to the target field occurs very quickly inside the DT. The Flex-DT design performs similarly well, deviating by only 1.1 V, although the distance required to reach the target value is 18 mm, longer than the resistive DT, but much shorter than the conventional stacked DT design (30 mm). It should be noted that a deviation of 1.1 V/mm is only 2.6% of the target field value and it converges to 1% compliance after 10 mm. The overlapping shielding electrodes' small electrode width (0.9 mm) and gap (0.3 mm) enable convergence to the target field in a comparable manner to the resistive glass DT. In the central region (2), all three designs sustain a highly homogeneous field at the target value. The field in the exit region (3) is more divergent than the entrance region due to the larger gap between the exit aperture and the Faraday plate. This is introduced to allow drift gas to enter the drift region, a necessity for IMS operation.

The resistive DT diverges from the ideal field gradient by a maximum of 4 V/mm and the divergence begins 20 mm away from the end of the tube. The divergence for the Flex-DT-IMS is 2.5 V/mm, substantially better than both other designs. The field diverges negatively with respect to the target value in the case of the resistive-DT and Flex-DT due to the gap between the Faraday and exit aperture being larger than the gap between the drift electrodes (0.9 mm v 0.3 mm). Whereas in the standard tube design the gap is smaller than the distance between the electrodes (0.9 mm v 1 mm), hence it diverges in a positive sense. Field deviations in the conventional design are considerably worse than both the Flex-DT and resistive-DT, yet are similar to those reported in other DT studies.[25,26,47]

In a standard DT configuration, it is well-known that ions entering the DT at the outer edge experience a slightly different field than ions traversing close to the central axis.[48] Proximity to electrodes and the comparatively small gap between electrodes causes the field to vary transversely, close to the perimeter of the drift region (Figure 2(b)). This undesirable attribute can lead to broadening of a detected ion packet's peak shape due to inherently different drift velocities. This effect can be mitigated by reducing the area of the Faraday plate detector thereby only sampling ions traveling in the central region (i.e., close to the central axis). The trade-off, though, leads to a loss of sensitivity, as a proportion of ions with the same cross-sectional area would be discharged on a grounded shielding electrode rather than measured on the Faraday plate. For the Flex-DT, due to the closely spaced electrodes and the overlapping arrangement, the field is extremely uniform even at distances relatively close to the electrodes. With this design it is possible to approach the linearity of the field inherent to resistive glass tube designs, yet manufactured at a fraction of the cost, while enabling higher sensitivity compared to conventional DTs due to an increased detection area. This is evident in Figure 2(a−c), whereby the electric field distribution for the three DTs is compared by taking their respective cross sections at the center of the tube.

https://dx.doi.org/10.1021/acs.analchem.0c01357
Anal. Chem. 2020, 92, 9104−9112

The resistive and flexible DTs are entirely consistent; however, the more standard DT configuration shows a noticeable variation of up to 0.8 V/mm (from center to outside edge).

Counter Gas Flow Double Glazing Arrangement: CFD Simulations. Conventional DT-IMS instruments contain at least one point of entry for the drift gas to enter and exhaust from the drift region. This process is an important and often overlooked factor[49] influencing IMS performance. Introducing temperature gradients that diverge significantly from the value for T or P used in eq 2 and K or T in eq 4 impacts the accuracy of K_0 and instrument resolution. The gas entry point creates discontinuities in atmospheric conditions within the DT. Relatively fast-moving gas expanding into a larger volume creates turbulence, localized cooling, nonuniform velocity profiles, and ultimately gas density differentials. The efficiency with which this process is managed can have a significant impact on performance.[50]

To minimize temperature and density gradients we employ a novel "double glazed" counter gas flow arrangement system that creates well-regulated temperature uniformity and drift gas velocity profile (Supporting Information Figure S3). As drift gas passes the desolvation and drift tube heaters it acquires thermal energy and efficiently preconditions the gas to the desired temperature before continuing through the gas entry corridor and into the drift tube. This preconditioning stage is accomplished without additional heating elements which would impose additional power requirements. A further benefit of the double-glazed arrangement is decoupling the Flex-DT-IMS assembly from the ambient environment.

CFD simulations were carried out to assess the performance of the counter gas flow arrangement in terms of its velocity profile and temperature distribution. Figure 3(a) shows the z-velocity profile for five different gas flow rates (1000, 800, 600, 400, and 200 mL/min) at the gas inlet boundary. For low flow rates, 200−600 mL/min, there is minimal deviation from a consistent velocity value throughout most of the DT. At 800−1000 mL/min, a significant velocity gradient is created along the DT. A small, low-pressure boundary layer forms on top of the Faraday plate due to higher gas velocity and the 360° opening (at the IMS inlet) creating a funneling effect (see Supporting Information Figure S4). Inrushing gas collides, pushing toward the IMS inlet with increasing force. This effect significantly interrupts the uniformity of the gas velocity profile at flow rates >800 mL/min, whereby the increased force results in acceleration of the gas to almost double the bulk velocity over several cm inside the DT. While this effect is nonideal, our results do compare favorably with other simulation studies describing the velocity profile of drift gas in a DT-IMS.[51,52] Notably, in both of these publications[51,52] a restricted drift gas entry orifice is located at the detector end which creates a higher-pressure gas flow entering the DT compared to our design whereby the gas is very well diffused prior to entering the DT.

Despite the difficulties in measuring the internal buffer gas temperature, a home-built test rig consisting of a miniature k-type thermocouple mounted to a linear stage was constructed to measure temperature at discrete 1 cm intervals inside the DT. The thermocouple head and wire diameter measured 0.6 mm, the gap between the B−N gate wires measured 0.8 mm, therefore, care was taken to ensure the delicate B−N gate and aperture wires were not damaged during the measurement process. Figure 3(b) displays measured and simulated temperatures within the Flex-DT-IMS for N_2 buffer gas flow

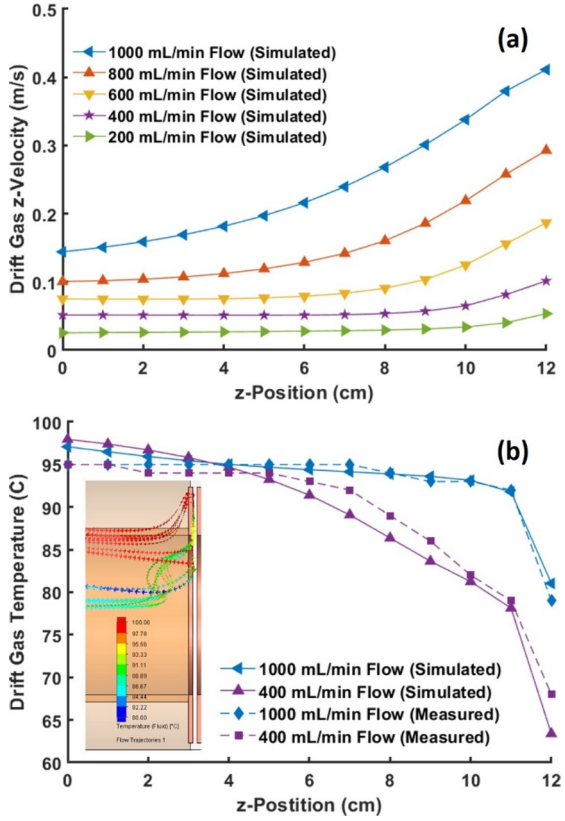

Figure 3. (a) Simulated drift gas z-velocity (m/s). (b) Simulated and measured drift gas temperatures (°C) at 1 cm intervals along the length of the drift tube. Insert is the drift gas flow lines colored to temperature in °C.

rates (1000 mL/min and 400 mL/min) at a set point temperature of 100 °C. For 1000 mL/min flow rate, the temperature along the tube is consistently a few degrees below the set point temperature and can consistently be accounted for by calibration. The temperature drop for the final cm of the tube accounts for less than 8% of the total length and is inconsequential in terms of its impact on the resolution and K_0 calculation. For a lower flow rate, 400 mL/min, a temperature deviation of 15 °C across 11 cm of DT length and a decrease of 10 °C in the final cm is observed in both simulated and measured data. The insert for Figure 3(b) shows the source of the problem, streamlines depicting the gas temperature as it enters the drift tube. As desired, the gas warms to 100 °C during its transit along the outside of the DT. As the gas moves through the orifice its passage is narrowed and it is subject to thermal contact with the end-cap. SI Figure S5 shows the simulated temperature of the solid material. The glass insulator and DT reach the required set point temperature of 100 °C, however, the large PTFE housing of the aperture grid and Faraday plate remain at ∼70 °C, see Supporting Information Figure S4. For lower flow rates, the time spent in contact with the end-cap and aperture grid is longer enabling thermal transfer to the insulating material to occur. It requires 8 cm of travel inside the tube before gas temperatures reach 100 °C. For all experiments reported, a gas velocity of 400 mL/min was used to take advantage of the highly stable velocity profile. Drift gas heating was set to 30 °C, this has the added benefit of increasing resolution.

Flex-DT-IMS: Resolution and Transmission Characteristics. To establish performance metrics for the Flex-DT-IMS,

https://dx.doi.org/10.1021/acs.analchem.0c01357
Anal. Chem. 2020, 92, 9104−9112

in conjunction with other elements of the IMS system, a voltage sweep experiment was performed (Figure 4). Iodine,

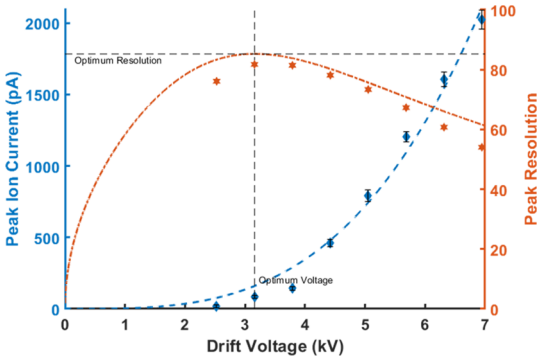

Figure 4. Peak ion current (left axis/blue color: diamonds = experiment; dashed = line of best-fit) and resolution (right axis/red color: stars = experiment; dashed = theory, eq 4) curves versus drift voltage (in kV) for 160 μs injection time. Dashed line (black color) labeled "Optimum Resolution" is plotted from eq 5.

with a measured K_0 = 1.71 cm^2/(V s), was employed as a model analyte due to the ease of ionization on account of its high electronegativity providing a large signal response from trace amounts of vapor. A small volume of iodine vapor was introduced in proximity to a corona discharge ion source at the IMS inlet. A constant ion injection width of 160 μs admitted ions into the DT region and the drift voltage was swept from 3.33 kV to 7.33 kV in 666.67 V increments. The resolution of each peak was determined using eq 3 and the result plotted in Figure 5. The experimental data closely follows the theoretical

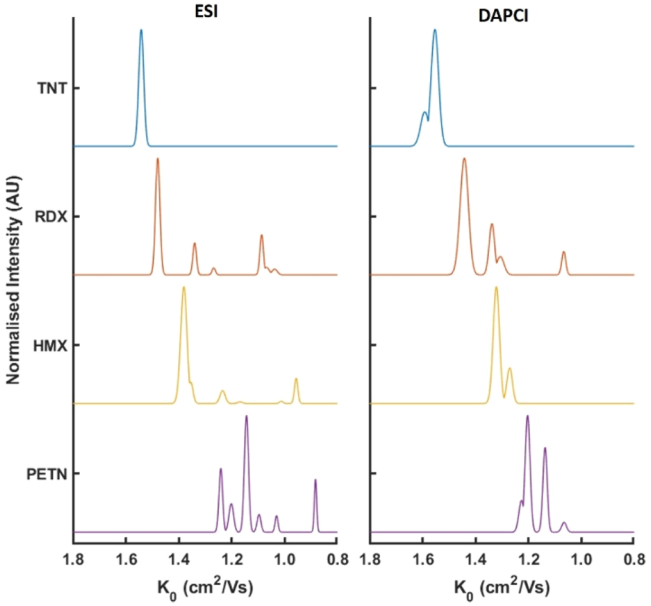

Figure 5. IMS spectra from 500 ng/mL concentration of TNT, RDX, HMX, and PETN (as labeled within the figure).

trendline from eq 4, with good agreement (R^2 = 0.9240). The ideality eq (eq 5), as derived by Kirk et al.,[13] is given as,

$$ideality = \frac{1}{26.4}\sqrt{\frac{R_{opt,meas}{}^2 T}{U_{opt,meas}}} \quad (5)$$

where $R_{opt,\,meas}$ is the measured resolution, T is the drift temperature and $U_{opt,\,meas}$ is the optimal drift voltage to acquire the optimal resolution. The measured resolution at the optimal drift voltage of 3159 V was 81.7 (Figure 4) which, compared to the ideal value of 85.2, indicates that the system has an ideality factor of 95.9%.

The slight divergence from ideal behavior is most likely due to the Bradbury–Nielsen (B–N) gating mechanism, rather than discontinuities in either the field or temperature gradient. The goodness of fit to the theoretical curve for the experimental parameters is evidence for the establishment of near ideal field conditions and the limitation imposed currently on resolution is most likely due to nonideal injection. Supplementary Figure S7 (see Supporting Information) shows the resolution versus gate opening time for a constant drift voltage of 4.5 kV and gate voltage of 60 V. The resolution increases almost linearly until ~300 μs where it begins to saturate as the gate injection imposed resolution limit is reached. While the B–N gate has been the workhorse of commercial and research instruments for many years, there are well-known limitations associated with the short injection times required to push the resolving power beyond 100.[21,53−55] To the best of our knowledge, all of the ultrahigh-resolution systems reported for DT-IMS have used a field switching gate rather than a B–N gate.

The transmission characteristics of the Flex-DT-IMS can be seen in Figure 4 (left-hand axis, blue diamonds). The transmission characteristics follow a first order power model fit to the transmission data with R^2 = 0.986. This result is in agreement with the well-known effect of increasing signal intensity when operating above the optimum drift voltage.[13] The raw data is depicted in the Supporting Information, Figure S6.

Analysis of Explosives (RDX, PETN, TNT, HMX) by DAPCI-IMS and ESI-IMS. To demonstrate the sensitivity and applicability of the Flex-DT-IMS, a series of experiments were performed analyzing standard explosive compounds RDX, TNT, HMX, and PETN. Representative spectra for 500 μg/mL of each explosive can be seen in Figure 5 for analysis with both DAPCI-IMS and ESI-IMS. A drift voltage of up to 8 kV was applied across the tube in each experiment with temperature set at 30 °C and pressure measured at 756.4 Torr.

TNT. Analysis of TNT under interrogation by DAPCI-IMS reveals two highly abundant peaks corresponding to K_0 values of 1.592 and 1.553 cm^2/(V s). The peak at 1.553 cm^2/(V s) is likely to correspond to the deprotonated ion, [TNT-H]$^-$, that is commonly reported in the literature.[5] This is in very close agreement with a recent study by Hauck et al. using a very high precision IMS instrument under similar temperature and pressure conditions with a reported K_0 for [TNT-H]$^-$ of 1.555 cm^2/(V s).[56] It is also well within the range that has been extensively reported elsewhere.[57−59] A further peak at 1.592 is potentially due to the loss of NO_2 as a result of thermal fragmentation. [TNT-NO_2]$^-$ has been reported previously in the literature as having a K_0 between 1.57 and 1.6.[5]

In ESI experiments, only a single highly abundant peak was captured at 1.549 cm^2/(V s) likely corresponding to the same deprotonated, [TNT-H]$^-$, anion. This is again similar to reports from the ESI-IMS literature for the detection of TNT.[4,60,61] A calibration curve for TNT (Supporting Information Figure S8) exhibited high linearity (R^2 = 0.9994) across the dynamic test range of 1–100 ng. A limit of detection (LOD) of 4.02 ng and a relative standard

https://dx.doi.org/10.1021/acs.analchem.0c01357
Anal. Chem. 2020, 92, 9104−9112

deviation (RSD) of 4.6% across the five data points is evidence of the linearity and repeatability of the Flex-DT-IMS design.

RDX. ESI interrogation of RDX provided a major identifying ion peak with a K_0 value of 1.48 $cm^2/(V\ s)$ which is in agreement with other reports.[5,60] A suspected dimer peak can be seen at 1.085 $cm^2/(V\ s)$, similar to that observed by Du et al.,[62] who identified an RDX dimer, $[2RDX+NO_2]^-$, with a K_0 of 1.05 $cm^2/(V\ s)$. RDX interrogation by DAPCI-IMS results in a major identifying peak at 1.44 $cm^2/(V\ s)$ and is within the range of reported values for RDX using corona discharge sources.[57,63] Two lower intensity peaks at 1.33 $cm^2/(V\ s)$ and 1.31 $cm^2/(V\ s)$ can also be seen in addition to a suspected dimer ion peak at 1.067 $cm^2/(V\ s)$.

HMX. ESI-IMS spectra of HMX can be characterized by a high intensity single dominant peak at K_0 = 1.39 $cm^2/(V\ s)$, a smaller suspected dimer peak located at 0.96 $cm^2/(V\ s)$ and several lower intensity ion peaks at 1.35 $cm^2/(V\ s)$, 1.23 $cm^2/(V\ s)$ and 1.02 $cm^2/(V\ s)$. This has agreement with a high resolution ESI-IMS study[4] that was able to determine HMX detection from two peaks at K_0 = 1.35 $cm^2/(V\ s)$ and 1.30 $cm^2/(V\ s)$. For DAPCI analysis, two highly abundant peaks at K_0 values of 1.32 $cm^2/(V\ s)$ and 1.27 $cm^2/(V\ s)$ were present.[62]

PETN. ESI-IMS spectra of PETN revealed five peaks across the range 1.241 $cm^2/(V\ s)$ to 1.09 $cm^2/(V\ s)$ with a dominant peak occurring at K_0 = 1.19 $cm^2/(V\ s)$. A potential dimer was also observed at 0.883 $cm^2/(V\ s)$. An IMS study using tandem mass analysis of PETN adducts[64] described a similar pattern with a mass-identified major peak corresponding to $[PETN\cdot NO_3]^-$ at K_0 = 1.21 $cm^2/(V\ s)$ alongside other identified adducts and molecular arrangements: $[PETN\cdot N_2O_2\cdot OH]^-$, $[PETN\cdot NO_2]^-$, $[PETN\text{-}H]^-$, $NO_2\cdot[PETN\text{-}H]^-$. A similar distribution of charge across multiple peaks in the PETN spectrum can be seen in the DAPCI spectra with K_0 values of 1.06, 1.14, 1.20, and 1.22 $cm^2/(V\ s)$, respectively. The most abundant ion peak at 1.20 $cm^2/(V\ s)$ corresponds closely with previous studies as do the other K_0 values observed.[62,63]

CONCLUSION

A novel Flex-DT-IMS has been designed and systematically characterized according to its key design features and operating parameters through simulation and experimental observations. The lightweight (<10 g) Flex-DT represents, theoretically, the minimum conceivable space arrangement possible. The bespoke "dog-leg" electrode arrangement allows shelf-shielding and shows great potential for a portable, low-cost and high performance IMS, constructed from a single PCB. The Flex-DT is capable of achieving a resolution metric in excess of 80, which places it into the category of high resolution.[17] This result is even more significant given the ease of assembly and cost to manufacture, which is a fraction of that required for a traditional DT design. This is a key building block toward future research endeavors, such as the establishment of a low-cost, portable and power-efficient IMS system suitable for high volume manufacture, to enable off-the-shelf analytical instrumentation for Internet of Things (IoT) measurements with high-speed connectivity for cloud-based data analytics. The Flex-DT is a critical building block toward an IoT network incorporating IMS technology that can enable stand-off, online vapor monitoring for explosives at key infrastructure.

Experimental data for the Flex-DT-IMS are supported by electrostatic and fluid dynamic field simulations, showing high consistency in terms of the electric field gradient, gas temperature profile and gas velocity vector field within the arrangement. Furthermore, we have demonstrated the applicability of the Flex-DT-IMS within a complete customized IMS system with comparable performance to other high-resolution instruments. The device is readily configurable for interfacing with a plethora of ambient ionization sources. Data is reported for the analysis of four common explosive compounds (TNT, RDX, HMX and PETN) using two different ion sources, ESI and, for the first-time, DAPCI, exhibiting good sensitivity (LOD for TNT, ~4 ng) and excellent linearity (R^2 > 0.999).

ASSOCIATED CONTENT

Supporting Information

The Supporting Information is available free of charge at https://pubs.acs.org/doi/10.1021/acs.analchem.0c01357.

Additional figures regarding methods, simulation and experimental data (PDF)

AUTHOR INFORMATION

Corresponding Author

Simon Maher − *Department of Electrical Engineering & Electronics, University of Liverpool, Liverpool L69 3GJ, U.K.*; orcid.org/0000-0002-0594-6976; Email: s.maher@liverpool.ac.uk

Authors

Barry L. Smith − *Department of Electrical Engineering & Electronics, University of Liverpool, Liverpool L69 3GJ, U.K.*

Cedric Boisdon − *Department of Electrical Engineering & Electronics, University of Liverpool, Liverpool L69 3GJ, U.K.*

Iain S. Young − *Institute of Integrative Biology, University of Liverpool, Liverpool L69 3BX, U.K.*

Thanit Praneenararat − *Department of Chemistry, Faculty of Science, Chulalongkorn University, Bangkok 10330, Thailand*; orcid.org/0000-0001-9165-2642

Tirayut Vilaivan − *Department of Chemistry, Faculty of Science, Chulalongkorn University, Bangkok 10330, Thailand*

Complete contact information is available at: https://pubs.acs.org/10.1021/acs.analchem.0c01357

Author Contributions

The manuscript was written through contributions of all authors. All authors have given approval to the final version of the manuscript.

Notes

The authors declare no competing financial interest.

ACKNOWLEDGMENTS

S.M. and B.L.S. acknowledge the gracious support of this work through the EPSRC and ESRC Centre for Doctoral Training on Quantification and Management of Risk & Uncertainty in Complex Systems & Environments (EP/L015927/1), supported by Q Technologies. SM also acknowledges the EPSRC (EP/R007500/1 and EP/R511729/1) and Newton Fund Institutional Links. In addition, we thank Mr Gareth Blacoe and Mr Paul Cross for their assistance with mechanical design and manufacture.

REFERENCES

(1) Maher, S.; Jjunju, F. P.; Taylor, S. *Rev. Mod. Phys.* **2015**, *87* (1), 113−135.

(2) Peng, L.; Hua, L.; Wang, W.; Zhou, Q.; Li, H. *Sci. Rep.* **2015**, *4*, 6631.
(3) Buryakov, I. *J. Anal. Chem.* **2011**, *66* (8), 674−694.
(4) Hilton, C. K.; Krueger, C. A.; Midey, A. J.; Osgood, M.; Wu, J.; Wu, C. *Int. J. Mass Spectrom.* **2010**, *298* (1), 64−71.
(5) Ewing, R. G.; Atkinson, D. A.; Eiceman, G. A.; Ewing, G. J. *Talanta* **2001**, *54* (3), 515−529.
(6) Khayamian, T.; Tabrizchi, M.; Jafari, M. T. *Talanta* **2006**, *69* (4), 795−799.
(7) Forbes, T. P.; Najarro, M. *Analyst* **2016**, *141* (14), 4438−4446.
(8) Seto, Y.; Hashimoto, R.; Taniguchi, T.; Ohrui, Y.; Nagoya, T.; Iwamatsu, T.; Komaru, S.; Usui, D.; Morimoto, S.; Sakamoto, Y.; Ishizaki, A.; Nishide, T.; Inoue, Y.; Sugiyama, H.; Nakano, N. *Anal. Chem.* **2019**, *91* (8), 5403−5414.
(9) Leaptrot, K. L.; May, J. C.; Dodds, J. N.; McLean, J. A. *Nat. Commun.* **2019**, *10* (1), 985.
(10) Lanucara, F.; Holman, S. W.; Gray, C. J.; Eyers, C. E. *Nat. Chem.* **2014**, *6*, 281.
(11) Jurneczko, E.; Barran, P. E. *Analyst* **2011**, *136* (1), 20−28.
(12) Verbeck, G. F.; Ruotolo, B. T.; Gillig, K. J.; Russell, D. H. *J. Am. Soc. Mass Spectrom.* **2004**, *15* (9), 1320−1324.
(13) Kirk, A. T.; Bakes, K.; Zimmermann, S. *Int. J. Ion Mobility Spectrom.* **2017**, *20*, 105−109.
(14) Adamov, A.; Mauriala, T.; Teplov, V.; Laakia, J.; Pedersen, C. S.; Kotiaho, T.; Sysoev, A. A. *Int. J. Mass Spectrom.* **2010**, *298* (1), 24−29.
(15) Dugourd, P.; Hudgins, R. R.; Clemmer, D. E.; Jarrold, M. F. *Rev. Sci. Instrum.* **1997**, *68* (2), 1122−1129.
(16) Hädener, M.; Kamrath, M. Z.; Weinmann, W.; Groessl, M. *Anal. Chem.* **2018**, *90* (15), 8764−8768.
(17) Kirk, A. T.; Bohnhorst, A.; Raddatz, C.-R.; Allers, M.; Zimmermann, S. *Anal. Bioanal. Chem.* **2019**, *411* (24), 6229−6246.
(18) Kirk, A. T.; Raddatz, C.-R.; Zimmermann, S. *Anal. Chem.* **2017**, *89* (3), 1509−1515.
(19) Manard, M. J.; Kemper, P. R. *Int. J. Mass Spectrom.* **2016**, *402*, 1−11.
(20) Chen, C.; Chen, H.; Li, H. *Anal. Chem.* **2017**, *89* (24), 13398−13404.
(21) Du, Y.; Wang, W.; Li, H. *Anal. Chem.* **2012**, *84* (13), 5700−5707.
(22) Kirk, A. T.; Kueddelsmann, M. J.; Bohnhorst, A.; Lippmann, M.; Zimmermann, S. *Anal. Chem.* **2020**, *92* (7), 4838−4847.
(23) Kirk, A. T.; Zimmermann, S. *Int. J. Ion Mobility Spectrom.* **2015**, *18* (1), 17−22.
(24) Eiceman, G. A.; Karpas, Z.; Hill, Jr, H. H. *Ion Mobility Spectrometry*; CRC press, 2013.
(25) Soppart, O.; Baumbach, J. I. *Meas. Sci. Technol.* **2000**, *11* (10), 1473−1479.
(26) Liu, X.; Li, S.; Li, M. *Int. J. Ion Mobility Spectrom.* **2012**, *15* (4), 231−237.
(27) Hauck, B. C.; Siems, W. F.; Harden, C. S.; McHugh, V. M.; Hill, H. H. *Int. J. Ion Mobility Spectrom.* **2017**, *20* (3), 57−66.
(28) Laprade, B., Use of Conductive glass tubes to create electric fields in ion mobility spectrometers. Use of Conductive glass tubes to create electric fields in ion mobility spectrometers 2005, *U.S. Pat. App.*US20140262971A1.
(29) Kwasnik, M.; Fernández, F. M. *Rapid Commun. Mass Spectrom.* **2010**, *24* (13), 1911−1918.
(30) Kwasnik, M.; Fuhrer, K.; Gonin, M.; Barbeau, K.; Fernández, F. M. *Anal. Chem.* **2007**, *79* (20), 7782−7791.
(31) Hollerbach, A.; Fedick, P. W.; Cooks, R. G. *Anal. Chem.* **2018**, *90* (22), 13265−13272.
(32) Drumheller, A., Tubular structure component with patterned resistive film on interior surface and systems and methods 2014, *U.S. Pat. App.*US2014262971A1.
(33) Jones, D. A., Self-shielding flex-circuit drift tube, drift tube assembly and method of making 2016, *U.S. Pat. App.* US9324550B1.
(34) Smith, B. L.; Smith, N. A.; Jjunju, F. P.; Young, I. S.; Vossebeld, J.; Casse, G.; Taylor, S.; Maher, S. *IEEE SENSORS* **2017**, 1−3.
(35) Reinecke, T.; Clowers, B. H. *HardwareX* **2018**, *4*, No. e00030.
(36) Barney, B. L.; Daly, R. T.; Austin, D. E. *Rev. Sci. Instrum.* **2013**, *84* (11), 114101.
(37) Bohnhorst, A.; Kirk, A. T.; Zimmermann, S. *Int. J. Ion Mobility Spectrom.* **2016**, *19* (2), 167−174.
(38) Bunert, E.; Kirk, A. T.; Käbein, O.; Zimmermann, S. *Int. J. Ion Mobility Spectrom.* **2019**, *22* (1), 21−29.
(39) Tridas, E. M.; Allemang, C.; Mast, F.; Anthony, J. M.; Schlaf, R. *J. Mass Spectrom.* **2015**, *50* (7), 938−943.
(40) Cooks, R. G.; Ouyang, Z.; Takats, Z.; Wiseman, J. M. *Science* **2006**, *311* (5767), 1566.
(41) Jjunju, F. P. M.; Maher, S.; Li, A.; Syed, S. U.; Smith, B.; Heeren, R. M. A.; Taylor, S.; Cooks, R. G. *Anal. Chem.* **2015**, *87* (19), 10047−10055.
(42) Cotte-Rodríguez, I.; Hernández-Soto, H.; Chen, H.; Cooks, R. G. *Anal. Chem.* **2008**, *80* (5), 1512−1519.
(43) Jjunju, F. P. M.; Maher, S.; Li, A.; Badu-Tawiah, A. K.; Taylor, S.; Graham Cooks, R. *J. Am. Soc. Mass Spectrom.* **2015**, *26* (2), 271−280.
(44) Yang, S.; Ding, J.; Zheng, J.; Hu, B.; Li, J.; Chen, H.; Zhou, Z.; Qiao, X. *Anal. Chem.* **2009**, *81* (7), 2426−2436.
(45) Ouyang, Y.; Liu, J.; Nie, B.; Dong, N.; Chen, X.; Chen, L.; Wei, Y. *RSC Adv.* **2017**, *7* (88), 56044−56053.
(46) Smith, B. L.; Hughes, D. M.; Badu-Tawiah, A. K.; Eccles, R.; Goodall, I.; Maher, S. *Sci. Rep.* **2019**, *9* (1), 7994.
(47) Lai, H.; McJunkin, T. R.; Miller, C. J.; Scott, J. R.; Almirall, J. R. *Int. J. Mass Spectrom.* **2008**, *276* (1), 1−8.
(48) Siems, W. F.; Wu, C.; Tarver, E. E.; Hill, H. H., Jr.; Larsen, P. R.; McMinn, D. G. *Anal. Chem.* **1994**, *66* (23), 4195−4201.
(49) Fernandez-Maestre, R. *Rev. Sci. Instrum.* **2017**, *88* (9), No. 096104.
(50) Fernandez-Maestre, R.; Meza-Morelos, D.; Wu, C. *Int. J. Mass Spectrom.* **2016**, *407*, 113−117.
(51) Han, F.; Du, Y.; Cheng, S.; Zhou, Q.; Chen, C.; Wang, W.; Li, H. *Int. J. Mass Spectrom.* **2012**, *309*, 13−21.
(52) Han, F.; Zhang, H.; Peng, L.; Li, H. *Int. J. Ion Mobility Spectrom.* **2016**, *19* (4), 219−226.
(53) Zühlke, M.; Zenichowski, K.; Riebe, D.; Beitz, T.; Löhmannsröben, H. G. *Int. J. Ion Mobility Spectrom.* **2017**, *20* (3), 67−73.
(54) Kirk, A. T.; Zimmermann, S. *Int. J. Ion Mobility Spectrom.* **2014**, *17*, 131−137.
(55) Kirk, A. T.; Grube, D.; Kobelt, T.; Wendt, C.; Zimmermann, S. *Anal. Chem.* **2018**, *90* (9), 5603−5611.
(56) Hauck, B. C.; Siems, W. F.; Harden, C. S.; McHugh, V. M.; Hill, H. H. *Rev. Sci. Instrum.* **2016**, *87* (7), No. 075104.
(57) Shahraki, H.; Tabrizchi, M.; Farrokhpor, H. *J. Hazard. Mater.* **2018**, *357*, 1−9.
(58) Kozole, J.; Levine, L. A.; Tomlinson-Phillips, J.; Stairs, J. R. *Talanta* **2015**, *140*, 10−19.
(59) Mullen, M.; Giordano, B. C. *Talanta* **2020**, *209*, 120544.
(60) Kanu, A. B.; Kumar, B. S.; Hill, H. H. *Int. J. Ion Mobility Spectrom.* **2012**, *15* (1), 9−20.
(61) Reid Asbury, G.; Klasmeier, J.; Hill, H. H., Jr. *Talanta* **2000**, *50* (6), 1291−1298.
(62) Du, Z.; Sun, T.; Zhao, J.; Wang, D.; Zhang, Z.; Yu, W. *Talanta* **2018**, *184*, 65−72.
(63) Lee, J.; Park, S.; Cho, S. G.; Goh, E. M.; Lee, S.; Koh, S.-S.; Kim, J. *Talanta* **2014**, *120*, 64−70.
(64) Filipenko, A. A.; Malkin, E. K. *J. Anal. Chem.* **2011**, *66* (14), 1464−1469.

https://dx.doi.org/10.1021/acs.analchem.0c01357
Anal. Chem. 2020, 92, 9104−9112